

# Comparative Study of AC and DC Solvers Based on Current and Power Distributions in a Submerged Arc Furnace



Y.A. TESFAHUNEGN, T. MAGNUSSON, M. TANGSTAD, and G. SAEVARSDOTTIR

This work discusses 3D models of current distribution in a three-phase submerged arc furnace that contains several components, such as electrodes, central arcs, craters, crater walls, and side arcs that connect electrodes and crater walls. A complete modeling approach requires time-dependent modeling of the AC electromagnetic fields and current distribution, while an approximation using a static DC approach enables a significant reduction in computational time. By comparing results for current and power distributions inside an industrial submerged arc furnace from the AC and DC solvers of the ANSYS Maxwell module, the merits and limitations of using the simpler and faster DC approach are estimated. The conclusion is that although effects such as skin effect and proximity are lost with the DC approach, the difference in the location of energy dissipation is within a 6 pct margin. The given inaccuracies introduced with an assumption about furnace configuration and physical properties are significantly more important for the overall result. Unless inductive effects are of particular interest, DC may often be sufficient.

<https://doi.org/10.1007/s11663-020-01794-z>

© The Minerals, Metals & Materials Society and ASM International 2020

## I. INTRODUCTION

SUBMERGED arc furnaces (SAFs) for silicon or ferrosilicon production are subject to two principal control mechanisms. On the one hand, it is the metallurgical control, which encompasses raw material selection, feeding, stocking, and tapping, and on the other, it is the electrical control, where the power dissipation is controlled by selecting the transformer set-point voltage as well as the phase currents or resistances. The electrical control strategy depends on the raw materials in the furnace, and the goal is to control the power dissipation through the current distribution. The electrical behavior in the furnace also affects the raw materials selected for given product specifications. There are no instruments/sensors that can measure the actual current distributions in the furnace directly. The practice in the industry is to operate the furnace based on the analysis of limited data at hand as well as by controlling the phase current or

resistance. Hence, developing a methodology that predicts current distribution is today's research question. Due to recent furnace dig-outs, which provide topography information and distribution of different material and intermediate compounds and the availability of computer resources, we are at the stage where we can develop reliable numerical models to predict the furnace behavior. This, in turn, will enhance our understanding of critical process parameters and allow us to control the furnace accurately.

The furnace is partitioned in various geometrical zones by taking into account the silicon furnace operation history. As reported by Tranell *et al.*,<sup>[1]</sup> different zones of the FeSi furnace have been described from industrial excavated furnaces. The results of the excavation published by Tranell *et al.*<sup>[2]</sup> find that the internal part of the furnace is divided into zones based on the materials and their degree of reduction. Myrhaug<sup>[3]</sup> reported similar features from an excavation on a pilot-scale furnace, operating around 150 kW. Mapping the material distribution gives a basis for quantifying the location-dependent physical properties of the charge materials such as electrical conductivity.

Developing a comprehensive numerical model of the SAF (submerged arc furnace) includes electrical, chemical, thermal, and fluid flow considerations. However, operational experience and results from the furnace dig-outs show that the material distribution in the furnace, and thus the location-dependent electrical characteristics, is extremely variable and dependent on

---

Y.A. TESFAHUNEGN and G. SAEVARSDOTTIR are with the Department of Engineering, Reykjavik University, Menntavegur 1, 101 Reykjavik, Iceland. Contact e-mail: yonatant@ru.is. T. MAGNUSSON is with the Stakksberg ehf, Stakksbraut 9, 230 Reykjanesbae, Iceland. M. TANGSTAD is with the Department of Materials Science and Engineering, Norwegian University of Science and Technology, 7491 Trondheim, Norway.

Manuscript submitted February 5, 2019.

Article published online February 18, 2020.

the operational history of the respective furnaces. Therefore, it is reasonable to address the electrical modeling, which can be based on dig-out results and material and temperature-dependent electrical data, separately from the rest of the multi-physics. In the regions of the furnace where the current passes and the metal-producing reactions occur, most materials are solid or semi-solid, so the transport of materials in the furnace is determined by convection from below combined with gravity. Fluid mechanics are useful for modeling tapping from the furnace, along with pressure and gas-flow through the charge or toward the tap-hole.

The issue of the best control strategy for the furnace is a very complex one. However, in industrial application, the existing controlling strategies for SAFs are mainly either current or resistance control.<sup>[4]</sup> Hence, in this study, we consider the electrical aspects, which require the electrical conductivity of the different zones of the furnace based on the excavation of furnaces. Some published research addresses this issue. Krokstad<sup>[5]</sup> outlined an experimental method and published data on the electrical conductivity of silicon carbide, and Vangskåsen<sup>[6]</sup> looked at the metal-producing mechanisms in detail. Molnas<sup>[7]</sup> and Nell<sup>[8]</sup> have also published data on dig-out samples and material analysis that are relevant. This does not mean, however, that there is sufficient conductivity data available at this time to map out the furnace completely; that work is still on-going and would be a prerequisite for developing a complete and accurate numerical model of the electrical aspects within the furnace. The improved and limited availability of physical properties, along with the enhanced information on the furnace interior layout, presents a unique opportunity to create a model that improves understanding of the current and power distributions in the system. Based on these results, furnace control strategies can be developed to enhance silicon recovery and energy efficiency.

Modeling the electrical aspects of SAF can be simplified by only considering a 2D domain that contains three electrodes or complicated by analyzing a 3D model that includes various parts of the furnace. In both cases, either a numerical DC (direct current) solver or AC (alternating current) solver can be utilized depending on the availability of computer resources. Palsson and Jonsson<sup>[9]</sup> used the FEM (finite element method) to analyze the skin and proximity effects in Soderberg electrodes for the FeSi furnace. In the paper, a cross-section of the furnace is modeled in 2D and solved to obtain a time-harmonic solution of AC currents in the electrodes. Barba *et al.*<sup>[10]</sup> used a 3D FE (finite element) model to define an equivalent electric circuit to control the operations of a submerged arc furnace. The electric circuit model parameters were calculated by the FE model. The FE model of the furnace was partitioned into different zones with different electrical conductivities. Tesfahunegn *et al.*<sup>[11,12]</sup> developed a 3D numerical furnace model that contains the electrodes, main arcs, side arcs, crater wall, crater, and other parts using the ANSYS Fluent electric potential solver (DC). The authors reported results for current distribution for a range of arcing configurations.

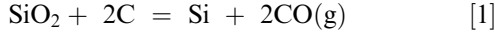
As a continuation of their work, they implemented a vector potential method using a user-defined function in the ANSYS Fluent environment to calculate dynamic current distributions.<sup>[13,14]</sup> That model only includes the electrodes and predicts skin and proximity effects. The same authors<sup>[15]</sup> extend their work on the model that has been developed in References 11, 12 to study the alternating current and power distributions using an eddy current solver (AC). Other researchers have developed different numerical models for SAF based on computational fluid dynamics (CFD) and the finite element method (FEM). Scheepers *et al.*<sup>[16,17]</sup> integrated a CFD model in dynamic modeling, a standard linear transfer function, in a SAF of phosphorus production. In the developed CFD model, the electrical and arc heating was modeled as volumetric heat sources. Herland *et al.*<sup>[18]</sup> studied proximity effects in large FeSi and FeMn furnaces using FEM. In their model, they included different parts of the furnaces. Diahnaut<sup>[19]</sup> used CFD to compute the electric field in SAF. The effect of contact resistance between two coke particles was studied in the paper before considering a full-scale furnace. The furnace was partitioned in layers to consider different materials, and no assumption was made on the current path. Bezuidenhout *et al.*<sup>[20]</sup> applied CFD on a three-phase electric smelting furnace to investigate the electrical characteristics, flow, and thermal response. They showed the relations among electrode positions, current distribution, and slag electrical resistivity. Moghadam *et al.*<sup>[21]</sup> developed an axis-symmetric two-dimensional mathematical model to describe the heat transfer and fluid flow in an AC arc zone of a ferrosilicon SAF. The model was able to predict temperature distribution, flow patterns, and current density on a melt surface. Darmana *et al.*<sup>[22]</sup> developed a modeling concept applicable to SAFs using CFD that considers various physical phenomena such as thermodynamics, electricity, hydrodynamics, heat radiation, and chemical reactions. Wang *et al.*<sup>[23]</sup> used a magnetohydrodynamic model to study a twin-electrode DC arc furnace designed for MgO crystal production. In their study, Maxwell and Navier-Stokes equations were coupled in ANSYS's working environment. Wang *et al.*<sup>[24]</sup> investigated the thermal behavior inside three different electric furnaces for MgO production. They developed 3D CFD models in FLUENT and compared the simulation results with measurements.

This article presents a comparative study of AC and DC solvers based on computations of current and power distributions inside an industrial submerged arc furnace for silicon metal production. As time-dependent AC is much more computationally demanding and time-consuming than the magnetostatic DC approach, it is worthwhile to study whether and when DC is sufficient to get the desired information. This comparison was done on a 3D model developed in ANSYS Maxwell<sup>[25]</sup> using the magnetostatic (DC) and eddy current (AC) solvers. The electrode, main arc, crater, crater wall, and side arc that connect the electrode and crater wall are taken into account for each phase. Other furnace parts such as the carbon block, steel shell, and aluminum block are also incorporated.

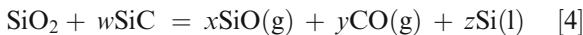
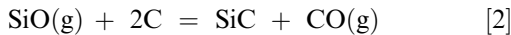
## II. THE PROCESS

In the silicon production process, the main ingredients, *i.e.*, quartz and carbon materials, commonly called the charge when mixed together, are fed into a submerged arc furnace. Three electrodes penetrate the charge from above. A three-phase 50-Hz AC electric current passes into the furnace through the electrodes and passes between the electrodes, dissipating heat in its path through materials in the furnace. Although the current flowing between the electrodes is distributed in the furnace, it is often described as a star point between the three electrodes.

The combined reaction that describes the stoichiometry for producing silicon is:



This reaction occurs through a series of sub-reactions at different temperatures. In turn, the charge properties are changed as intermediary reaction products are formed as shown in Eqs. [2] and [3], thus the location dependent physical properties in the domain. The current passes from one electrode to another through a number of pathways. It can pass directly from the electrode to the charge materials that are of limited conductivity. Further down in the furnace, the current will pass to highly conductive carbide material or directly to the metal product through electric arcs, which consist of thermal plasma of temperature in the range of 10,000 K to 25,000 K.<sup>[26]</sup> The arcing provides heat for the energy-consuming silicon-producing Reaction [4], which requires temperature > 1900 °C for good silicon recovery as its stoichiometry is temperature dependent. The SiC-forming reaction and SiO(g) condensation Reactions [2] and [3] take place at a lower temperature higher up in the furnace; see Schei *et al.*<sup>[27]</sup>.



It is vital for the silicon recovery in this process that there is a balance between the high-temperature Reactions [4] and low-temperature Reactions [2] and [3]. To drive Reactions [2] and [4], a certain heat should be released in the raw-material charge and sufficient heat through arcing, respectively. In the silicon process, it is the electric arc that creates a sufficiently high temperature, so adequate arcing is important for good silicon recovery.

## III. COMPUTATIONAL MODEL

In this section, we describe the mathematical modeling, furnace geometry, material properties, mesh generation, and boundary conditions.

### A. Mathematical Modeling

This work is mainly focused on the electrical characteristics of a submerged arc furnace. Magnetostatic (DC) and eddy current solvers (AC) are used to develop a 3D electrical model in ANSYS Maxwell.<sup>[25]</sup> The magnetostatic solver will capture neither the time-dependent effects nor the induction of the magnetic field. It solves static magnetic fields by DC current flowing through a conductor. The magnetostatic solver solves the following Maxwell equations<sup>[25]</sup>:

$$\nabla \times \mathbf{H} = \mathbf{J} \quad [5]$$

$$\nabla \cdot \mathbf{B} = 0 \quad [6]$$

$$\mathbf{B} = \mu_0 \mu_r(\mathbf{H}) \cdot \mathbf{H} \quad [7]$$

where  $\mathbf{H}$ ,  $\mathbf{B}$ ,  $\mathbf{J}$ , and  $\mu$  are the magnetic field, magnetic flux density, current density, and magnetic permeability, respectively. The magnetic permeability is typically given by  $\mu = \mu_r \mu_0$ , where  $\mu_0 = 4\pi \times 10^{-7}$  [H/m] is the constant magnetic permeability of the vacuum and  $\mu_r$  [-] is the relative magnetic permeability. The eddy current solver is an efficient way to solve for the time-dependent magnetic field assuming a harmonic field and is suitable for low-frequency devices and phenomena. It solves sinusoidally varying magnetic fields in the frequency domain. The frequency-domain solution assumes frequency to be the same throughout the domain, but the phase may differ. Induced fields such as skin and current proximity effects are captured. It is a quasi-static solver, as it assumes periodicity. The time-dependent Maxwell equations under these constraints can be simplified to the following equation for the magnetic field,  $\mathbf{H}$ , which the solver is based on Reference 25:

$$\nabla \times \left( \frac{1}{\sigma + j\omega\epsilon} \nabla \times \mathbf{H} \right) = -j\omega\mu\mathbf{H} \quad [8]$$

where  $\sigma$ ,  $\omega$ , and  $\epsilon$  are electrical conductivity, circular frequency, and electrical permittivity. Once the equations are solved, the electric field ( $\mathbf{E}$ ) and the electric current density ( $\mathbf{J}$ ) are calculated using Faraday's and Ampere's laws. Also,  $\mathbf{J}$  and  $\mathbf{E}$  are related by Ohm's law. The equations are solved by the finite element method.

### B. Furnace Geometry and Material Properties

In this article, we have considered the same industrial furnace as reported in References 11, 12, 15, operating at an AC frequency of 50 Hz, and its schematic diagram is shown in Figure 1, which is adapted from Reference 11. Due to the proprietary right, the dimensions and details of the furnace are not indicated in the figure. The computational domain is partitioned into different zones based on the material properties. It consists of the furnace lining, three electrodes, charge, molten material,

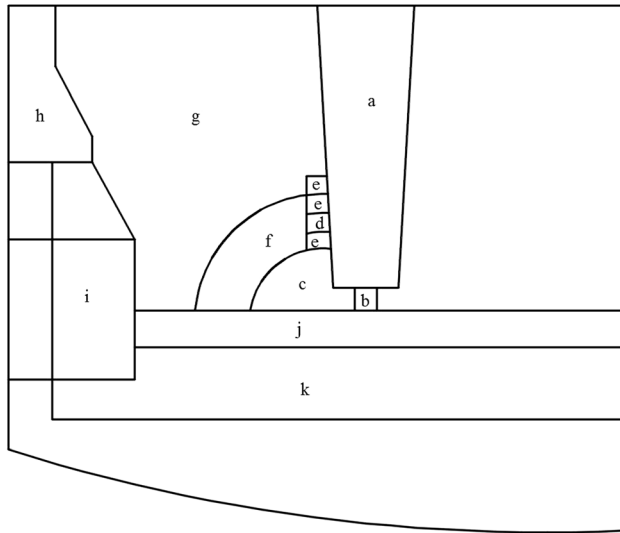


Fig. 1—Schematic of the industrial silicon SAF with different zones: (a) electrode, (b) arc, (c) crater, (d) side arc, (e) gap, (f) carbide, (g) charge, (h) alumina brick, (i) carbon block and carbide, (j) molten material, and (k) carbon block. Adapted from [11], with permission.

three arcs below electrodes, side arcs, and three craters with crater walls made of carbides. The geometry of each electrode is considered a truncated right conical shape. The base of the cone is the top surface of the electrode equal to the electrode radius. A change in the slope of the slant height changes the radius of the bottom surface of the electrode. It is assumed that several concentrated side arcs are distributed around the circumference of the electrodes near the tip of the electrodes, and the circular distances between each side arc are held constant. With this configuration, the number of side arcs increases linearly with the circumference of the electrode.

In Figure 1, [11] a section of the furnace and an electrode are shown. For each phase, two types of arcs are introduced: the main arc, burning below the electrode, with an arc length of 10 cm and a diameter of 5 cm,<sup>[28]</sup> and some shorter side arcs connecting the crater wall to the side of the electrode. The curvature of the three crater walls is assumed to be a circular section with a diameter of 100 cm.<sup>[29]</sup> The electrical conductivity of each zone is assigned based on an industrial excavated furnace,<sup>[2]</sup> and their value is taken from various literature sources and summarized in Table I.

### C. Mesh Generation and Boundary Conditions

The primary input of any computational method is the grid or mesh of the domain. The way the mesh is generated has a significant influence on the runtime and memory use of simulation as well as the accuracy and stability of the solution. There are two approaches to generate grids, *i.e.*, structured and unstructured meshes. Structured meshes are formed of regular lattices, and unstructured grids are formed of an arbitrary collection of elements. Generating structured mesh is a time-intensive task for complex domains. However, complex geometries can be meshed with great flexibility using an

Table I. Electrical Conductivity of Different Zones

Zones	Electrical Conductivity [S/m]
Electrode <sup>[5]</sup>	225,000
Arc <sup>[29]</sup>	7000
Crater	$1e^{-14}$
Carbide <sup>[5]</sup>	400
Charge	0.15, 15
Molten Material <sup>[30]</sup>	1,388,900
Carbon Block <sup>[5]</sup>	225,000
Alumina Brick	$1e^{-14}$
Steel Shell <sup>[18]</sup>	$6.3e^{+10}$

unstructured method. Since the furnace geometry is very complex and has several parts, the mesh is generated using the unstructured approach for both the DC and AC solvers. We utilize an adaptive mesh refinement algorithm for the material volumes described in Section III-B. This type of meshing technique provides automated mesh refinement capability based on reported energy error in simulation.

The model boundary conditions were imposed based on the positions of the surfaces in the model. Two types of boundary conditions are required, *i.e.*, the natural and Neumann. The natural boundary condition is used for the interface between objects. It describes the natural variation from one material to the next, as defined by the material property. The Neumann boundary condition is applied for the exterior boundary of the solution domain, and flux cannot penetrate, and the  $\mathbf{H}$  field is tangential to the boundary. To impose appropriate boundary conditions on the  $\mathbf{H}$  field, a large air-filled far-field is modeled around the furnace. A current of  $I_{\text{rms}} = 99\text{ kA}$  is imposed on the top surfaces of the three electrodes. In the AC cases, the phase shift between electrodes is 120 deg. Representative mesh and boundary conditions are shown in Figure 2.

## IV. NUMERICAL CASES

In this section, we determine the current and power distributions inside the furnace described in Section III-B as well as other parameters, such as the resistance and voltage of the system. We consider four factors. The first factor is the type of solver with two levels (DC and AC). The second factor is the number of side arcs with two levels (8 and 14), the third aspect is the charge conductivity with two levels (0.15 and 15 S/m). The last element is the consideration of the main arcs with two levels (with main arcs and without main arcs). Hence, a total of 16 simulation cases have been performed. For discussion purposes, we group them into two categories based on the fourth factor. We only vary the other three factors, *i.e.*, the type of solver, number of side arcs, and charge conductivity. The two categories are summarized in Table II.

For all cases, the phase current has the same value. This means that with changing domain configuration, the total resistance changes and thus the voltage of the system. Some of the cases represent realistic phase



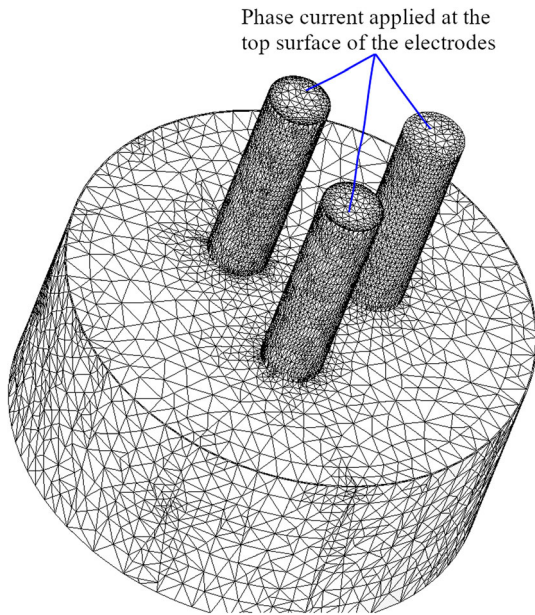


Fig. 2—Sample mesh and boundary conditions.

**Table II. Two Simulation Groups for DC and AC Solvers**

Category	Number of Side Arcs		Charge Conductivity	
	8	14	0.15 S/m	15 S/m
Main Arcs	✓	✓	✓	✓
No Main Arcs	✓	✓	✓	✓

resistance in the system while others do not; the goal with this effort is to gain a qualitative understanding of the governing mechanisms for the current and power distributions in the system.

Since the results that are required for this study are not directly obtained from the simulation, we need to perform post-processing. The current is calculated from the current density by integrating on the surface of interest. The power density,  $p[\text{W}/\text{m}^3]$ , is given by  $p = |\mathbf{J}|^2/2\sigma$ , where  $\mathbf{J}$  is the amplitude of the current vector. By integrating the power density over the different material domain and the entire furnace, we obtain power,  $P[\text{MW}]$ . Once the power of the furnace is calculated, the resistance ( $R$ ) of the system can be calculated.

#### A. Grid Convergence and Simulation Time

For all cases, the simulations were performed by an adaptive meshing algorithm using energy error as a convergence criterion and the error set to 2 pct.

Figure 3 shows the grid convergence of different cases with charge conductivity of 0.15 S/m. For the cases shown, four iterations are required to converge. In AC cases, the initial errors are higher than their corresponding DC cases. Moreover, the first iteration starts at

higher initial mesh for the DC solver and has a faster convergence rate compared with the AC solver. In Table III, the simulation time for all cases is provided. The minimum simulation time ratio between AC and DC is about 1.2, and the maximum value is around 2.5. As Figure 3 shows, the number of elements of the converged mesh of the DC solver is  $\sim 1.3$  times that of the AC solver. This means that for the same number of elements, the simulation time ratio between the AC and DC solvers would be even higher than shown in Table III.

#### B. Current Distributions

Figures 4(a) and (b) shows the current density from the AC and DC solvers, respectively, at the top of the electrode cross sections. In the AC result, the distribution is non-uniform on the three electrodes because of skin and proximity effects, whereas in the DC case the distribution is uniform. The current is forced to accumulate on the surface of the electrodes because of the skin effect and only on one side because of the proximity effect.

Figure 5 shows the total current through the electrode and the main arc at different heights of the furnace. The vertical axis is a normalized current, which is the fraction of the phase current in the electrode and arc. The horizontal axis is a dimensionless furnace height, which is the ratio between a given height and the total height of the furnace. In this article, we define the total height of the furnace from the bottom of the furnace to the top of the electrodes. In Figure 5(a), the main arc is considered, whereas in Figure 5(b) it is not included using the AC solver. Figures 5(c) and (d) shows the results from the DC solver. In all figures, the charge conductivity and number of side arcs vary, as shown in Table II. Irrespective of the magnitude of reduction, the current is decreasing from the top of the electrode to the bottom as the charge conductivity increases. Moreover, the current passed to the main arc (Figures 5(a) and (c)) is also decreased as the number of side arcs is increased. The total current distributions from AC and DC solvers are similar. Hence, for the initial estimation of the current distributions, it suffices to use the DC solver, and the AC solver can be used for further refinement to analyze effects such as skin and proximity effects. The other aspect we have investigated is that the current distributions change in the side arcs. Table IV shows the change in the current distribution in the side arcs. The tabulated values are the difference between the maximum and minimum current values of the side arcs. The maximum deviation is  $< 0.5$  pct compared with the total applied current. The variation may come from the fact that each side arc does not have an equal number of elements.

#### C. Power Distributions

The power in all components of the furnace is calculated according to the method described at the beginning of Section IV. Tables V and VI show the power distributions in different zones for 8 and 14 side

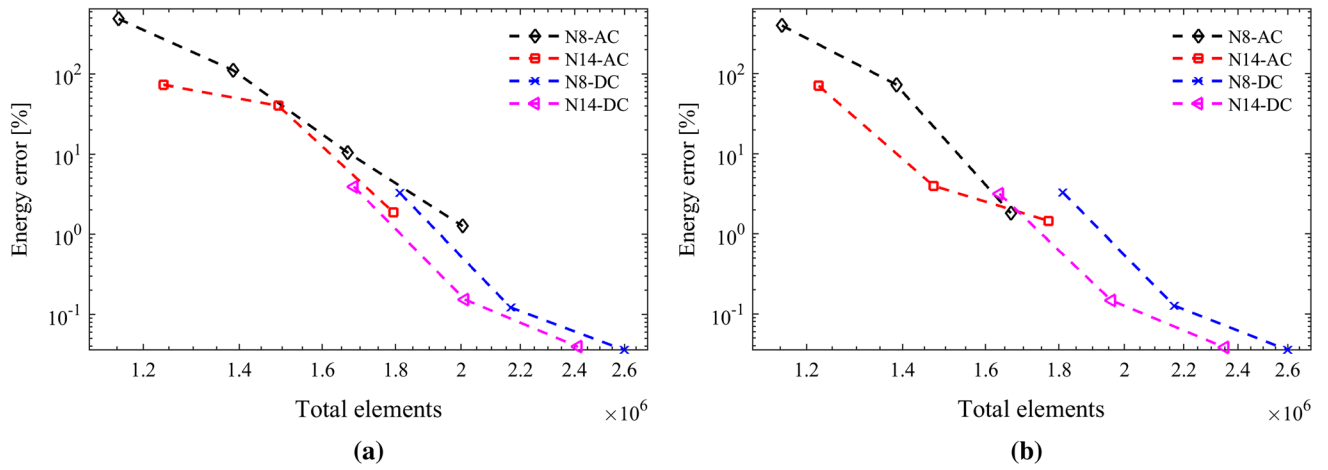


Fig. 3—Grid convergence based on energy percentage error for different cases with charge conductivity of 0.15 S/m. (a) With the main arc and (b) without the main arc.

Table III. Simulation Time

Cases	With Main Arcs				No Main Arcs			
	Charge Cond. 0.15		Charge Cond. 15		Charge Cond. 0.15		Charge Cond. 15	
	DC [min]	AC [min]	DC [min]	AC [min]	DC [min]	AC [min]	DC [min]	AC [min]
NsideArcs_8	116	240	103	252	127	152	102	244
NsideArcs_14	96	209	103	142	88	153	89	116

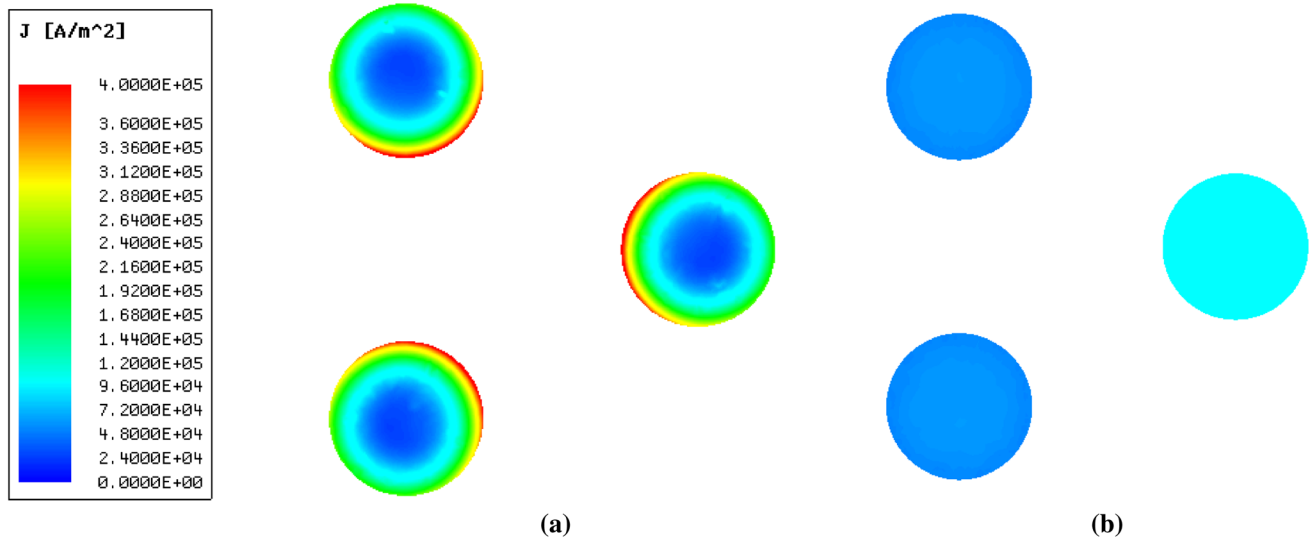


Fig. 4—Current density in the electrode top cross-section: (a) AC solver and (b) DC solver.

arcs with and without main arcs. The numbers that are shown in parentheses are the percentage of the total power in the respective cases. As there is uncertainty about the physical properties of the charge materials, it was decided to estimate the sensitivity to the electrical properties for the charge. All cases are modeled for two-charge conductivities, two orders of magnitude

higher than the other. When the main arcs are included and charge conductivity is low, most of the power is accumulated in the main arcs and crater wall, while some power is deposited in the remaining zones. However, when the charge conductivity is changed by two orders of magnitude, the power in the charge is increased by the same order of magnitude while

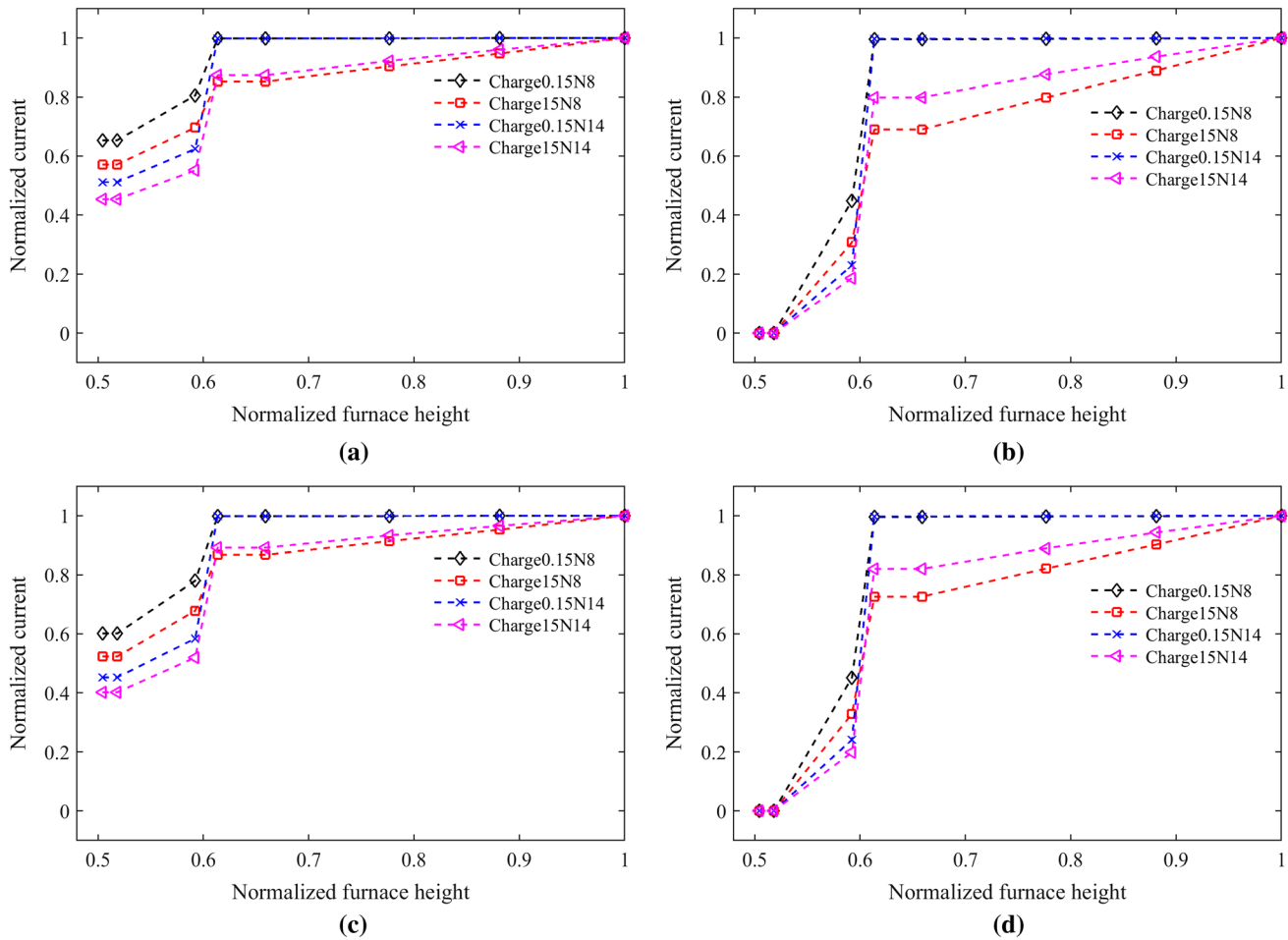


Fig. 5—Normalized current passing through electrode and main arc as a function of normalized height from the furnace bottom to the top of electrodes: (a) AC solver with main arc, (b) AC solver without main arc, (c) DC solver with main arc, and (d) DC solver without main arc.

decreasing in the main arcs, crater wall, electrodes, and others. Nevertheless, the power dissipation in the charge is only around 13 pct of the total heat dissipation. Without the main arcs, we can see the same trend except for no power in the main arcs. Without the main arc, the charge power dissipation reaches 25 pct of the total power dissipation for the high-charge conductivity cases. Comparing the DC and AC solvers, with few exceptions, the AC power in each component is higher than the DC power; it is especially highly pronounced in the electrodes in all simulation cases. This is mainly due to the skin and proximity effects captured with the AC solver, as these effects will lead to significantly increased localized current densities. The general trend is that the total AC power in the furnace is higher than the DC power by between 3 and 6 pct.

#### D. Resistance of the Furnace

In these simulations, it was decided to use tabulated physical properties for materials and then study the influence of different configurations rather than adapting the configurations and properties to the actual furnace operating resistance. Thus, for some of the

simulations resistances agree with the actual furnace, while others are quite different. Table VII shows the total resistance of the system for all cases. Having main arcs shows that the resistance of the system is sensitive to the change of charge conductivity and the number of side arcs. Without the main arcs, the resistance in the furnace is increased by 60 to 150 pct compared with the corresponding simulation cases (Table VII). Most furnaces are operated to strive toward constant resistances (sometimes through a current set point). The variations in conductivity conditions in the furnace are met by moving the electrodes up and down. From these simulations, we see how the resistance can change as either the conductivity of the charge is changed, the number of side arcs changed and the main arc included or not. In all simulation cases, we have assumed that the charge conductivity is uniform. In a real furnace, however, the charge conductivity is increasing as it moves from the top of the furnace to the bottom. Overall, the trend that can be observed is that increasing the system conductivity will result in a reduction of the system resistance. The most significant difference in results from the AC and DC simulations is that AC resistance is 3 to 7 pct higher than the DC resistance.

**Table IV. Current Distribution Change in the Side Arcs**

Cases	With Main Arcs				No Main Arcs			
	Charge Cond. 0.15		Charge Cond. 15		Charge Cond. 0.15		Charge Cond. 15	
	DC [kA]	AC [kA]	DC [kA]	AC [kA]	DC [kA]	AC [kA]	DC [kA]	AC [kA]
NsideArcs_8	0.0281	0.1073	0.0401	0.0924	0.0329	0.2251	0.0891	0.0997
NsideArcs_14	0.0219	0.1218	0.0680	0.1194	0.0656	0.1472	0.0865	0.2121

**Table V. Power Distributions in Different Zones for the Eight Side Arc Setup**

Zones	With Main Arcs				No Main Arcs			
	Charge Cond. 0.15		Charge Cond. 15		Charge Cond. 0.15		Charge Cond. 15	
	DC [MW] (pct)	AC [MW] (pct)	DC [MW] (pct)	AC [MW] (pct)	DC [MW] (pct)	AC [MW] (pct)	DC [MW] (pct)	AC [MW] (pct)
Electrode	1.06 (3.16)	2.30 (6.56)	0.94 (3.21)	2.13 (6.84)	0.86 (1.05)	2.06 (2.42)	0.72 (1.20)	1.82 (2.94)
Main Arcs	19.38 (57.82)	19.63 (56.02)	14.67 (50.17)	14.79 (47.50)	0.00 (0.00)	0.00 (0.00)	0.00 (0.00)	0.00 (0.00)
Side Arcs	0.76 (2.27)	0.74 (2.11)	0.57 (1.95)	0.56 (1.80)	4.78 (5.83)	4.76 (5.60)	2.54 (4.22)	2.49 (4.02)
Crater Wall	12.22 (36.46)	12.14 (34.65)	9.25 (31.63)	9.51 (30.54)	76.07 (92.73)	77.75 (91.47)	40.60 (67.53)	40.72 (65.70)
Charge Others	0.05 (0.15)	0.05 (0.14)	3.77 (12.89)	4.01 (12.88)	0.30 (0.37)	0.32 (0.38)	16.25 (27.03)	16.89 (27.25)
Total	33.52	35.04	29.24	31.14	82.03	85.00	60.12	61.98

**Table VI. Power Distributions in Different Zones for the 14 Side Arc Setup**

Zones	With Main Arcs				No Main Arcs			
	Charge Cond. 0.15		Charge Cond. 15		Charge Cond. 0.15		Charge Cond. 15	
	DC [MW] (pct)	AC [MW] (pct)	DC [MW] (pct)	AC [MW] (pct)	DC [MW] (pct)	AC [MW] (pct)	DC [MW] (pct)	AC [MW] (pct)
Electrode	0.80 (3.16)	2.04 (7.62)	0.74 (3.29)	1.94 (8.10)	0.68 (1.50)	1.88 (3.98)	0.63 (1.70)	1.77 (4.54)
Main Arcs	10.99 (43.47)	11.13 (41.58)	8.66 (38.49)	8.71 (36.38)	0.00 (0.00)	0.00 (0.00)	0.00 (0.00)	0.00 (0.00)
Side Arcs	0.48 (1.90)	0.48 (1.79)	0.39 (1.73)	0.36 (1.50)	1.62 (3.57)	1.62 (3.43)	1.09 (2.94)	1.07 (2.74)
Crater Wall	12.95 (51.23)	12.96 (48.41)	10.19 (45.29)	10.17 (42.48)	42.98 (94.69)	43.54 (92.23)	28.40 (76.69)	28.81 (73.85)
Charge Others	0.03 (0.12)	0.03 (0.11)	2.50 (11.11)	2.63 (10.99)	0.10 (0.22)	0.11 (0.23)	6.89 (18.61)	7.30 (18.71)
Total	25.28	26.77	22.50	23.94	45.39	47.21	37.03	39.01

**Table VII. Resistance of the Furnace**

Cases	With Main Arcs				No Main Arcs			
	Charge Cond. 0.15		Charge Cond. 15		Charge Cond. 0.15		Charge Cond. 15	
	DC [mΩ]	AC [mΩ]	DC [mΩ]	AC [mΩ]	DC [mΩ]	AC [mΩ]	DC [mΩ]	AC [mΩ]
NsideArcs_8	1.14	1.19	0.99	1.06	2.79	2.89	2.04	2.11
NsideArcs_14	0.86	0.91	0.77	0.81	1.54	1.61	1.26	1.33



## V. CONCLUSIONS

This article presents computations of current and power distributions inside an industrial submerged arc furnace for silicon production. Magnetostatic (DC) and harmonic eddy current (AC) solvers are used to develop the 3D electrical model in ANSYS Maxwell. Electrodes, main arcs, craters, crater walls, and side arcs that connect the electrode and crater wall are considered for each phase. In this article, the current distributions in the electrodes and main arcs and the power distributions in different parts of the furnace are simulated for configurations with varying charge conductivities and the number of side arcs and inclusions, or not, of the main arcs. It was observed for both solvers that the resistance of the furnace is sensitive to all of these changes. When the main arcs are burning against well-conducting metal-containing materials, most of the power is accumulated in the main arcs and crater wall for both high- and low-charge conductivities. It is the conductivity in the crater wall that determines the resistance in the volume at the side arc attachment and limits the side arc current. Thus, without main arcs, a significant portion of the power is placed in the crater and charge depending on the charge conductivity value, but the overall resistance in the system is unrealistically high for the material properties used in these models. The comparison shows that the DC solver gives results quickly with approximately 3 to 6 pct error as compared with the AC results. The difference comes from the induced skin and proximity effects that are not captured by the DC solver. Hence, for an initial estimation of the current and power distributions, it suffices to use the DC solver, and the AC solver can be used for further refinement to analyze effects such as skin and proximity effects.

## ACKNOWLEDGMENTS

The Icelandic Technology development fund is acknowledged for their funding of this work.

## REFERENCES

1. G. Tranell, M. Andersson, E. Ringdalen, O. Ostrovski, and J.J. Stenmo: *INFACON XII*, 2010, pp. 709–15.
2. M. Tangstad, M. Ksiazek, and J.E. Andersen: *Silicon for the Chemical and Solar Industry XII*, 2014, Trondheim, Norway, June 24–27.
3. E.H. Myrhaug: Ph.D. thesis, NTNU, 2013.
4. A.S. Hauksdottir, A. Gestsson, and A. Vesteinsson: *Control Eng. Pract.*, 2002, vol. 20, pp. 457–63.
5. M. Krokstad: MSc-thesis NTNU, 2014.
6. J. Vangskåsen: MSc. thesis, NTNU, 2012.
7. H. Mølnås: *Investigation of SiO condensate formation in the silicon process*, Project report in TMT 4500, NTNU, Norway, 2010.
8. J. Nell and C. Joubert C: *INFACON XIII*, 2013, pp. 265–71.
9. H. Palsson and M. Jonsson: Finite element analysis of proximity effects in Soderberg electrodes. <https://www.hi.is/~magnusj/ritverk/proximit.pdf>, Accessed 28 Oct 2019.
10. P.D. Barba, F. Dughiero, M. Dusi, M. Forzan, M.E. Mognaschi, M. Paioli, and E. Siena: *Int. J. Appl. Electromagn. Mech.*, 2012, vol. 20, pp. 555–61.
11. Y.A. Tesfahunegn, T. Magnusson, M. Tangstad, and G. Saevarsdottir: *J. S. Afr. Inst. Min. Metall.*, 2018, Ser. 6, vol. 118, pp. 595–00.
12. Y.A. Tesfahunegn, T. Magnusson, M. Tangstad, and G. Saevarsdottir: in *CFD Modeling and Simulation in Materials Processing*, The Minerals, Metals & Materials Series, L. Nastac, K. Pericleous, A. Sabau, L. Zhang, B. Thomas, eds., Springer, Cham, 2018, pp. 175–85.
13. Y.A. Tesfahunegn, T. Magnusson, M. Tangstad, and G. Saevarsdottir: in *Computational Science—ICCS 2018. ICCS 2018. Lecture Notes in Computer Science*, Y. Shi et al. eds., vol. 10861. Springer, Cham, pp. 518–27.
14. Y.A. Tesfahunegn, T. Magnusson, M. Tangstad, and G. Saevarsdottir: *IEEE MTT-S International Conference on Numerical and Electromagnetic and Multiphysics Modeling and Optimization*, Reykjavik, Iceland, 08–11 Aug 2018.
15. Y.A. Tesfahunegn, T. Magnusson, M. Tangstad, and G. Saevarsdottir: *Materials Processing Fundamentals. TMS 2019*, 2019.
16. E. Scheepers, Y. Yang, M.A. Reuter, and A.T. Adema: *Miner. Eng.*, 2006, vol. 19, pp. 309–17.
17. E. Scheepers, A.T. Adema, Y. Yang, and M.A. Reuter: *Miner. Eng.*, 2006, vol. 19, pp. 1115–25.
18. E.V. Herlanda, M. Sparta, and S.A. Halvorsen: *J. S. Afr. Inst. Min. Metall.*, 2018, Ser. 6, vol. 118, pp. 607–18.
19. M. Dhainaut: *INFACON X*, 204, pp. 605–13.
20. J.J. Bezuidenhout, J.J. Eksteen, and S.M. Bardshaw: *Minerals Engineering*, 2009, Ser. 11, vol. 22, pp. 995–06. <https://doi.org/10.1016/j.mineng.2009.03.009>.
21. M. M. Moghadam, S. H. Seyedein, and M.R. Aboutalebi: *J. Iron Steel Res. Int.*, 2010, vol. 17, pp. 14–18.
22. D. Darmana, J.E. Olsen, K. Tang, and E. Ringdalen: *The Ninth International Conference on CFD in the Minerals and Process Industries CSIRO*, Melbourne, Australia, 10–12 Dec 2012.
23. Z. Wang, N.H. Wang, and T. Li: *J. Mater. Process. Technol.*, 2011, vol. 211, pp. 388–95.
24. Z. Wang, Y. Fu, N. Wang, and L. Feng: *J. Mater. Process. Technol.*, 2014, vol. 214, pp. 2284–91. <https://doi.org/10.1016/j.jmatprotec.2014.04.033>.
25. Maxwell, ver. 18.0 ANSYS Inc., Southpointe, 275 Technology Drive, Canonsburg, 2018.
26. G.A. Saevarsdottir, J. Bakken, V. Sevastyanenko, and Gu Liping: *INFACON IX*, 2001, pp. 253–63.
27. A. Schei, J.K. Tuset, and H. Tveit: *Production of High Silicon Alloys*, Tapir Forlag, Trondheim, 1998.
28. G. Saevarsdotti, and J.A. Bakken: *INFACON XII*, 2010, pp. 717–28.
29. G.A. Saevarsdottir: Ph.D. thesis, NTNU, 2002.
30. H. Sasaki, A. Ikari, K. Terashima, and S. Kimura: *Jpn. J. Appl. Phys.*, 1995, vol. 34, pp. 3426–31. <https://doi.org/10.1143/JJAP.34.3426>.

**Publisher's Note** Springer Nature remains neutral with regard to jurisdictional claims in published maps and institutional affiliations.